B. Bal[1]
Department of Mechanical Engineering,
Kyushu University,
Nishi-ku 819-0395, Fukuoka, Japan;
Department of Mechanical Engineering,
Abdullah Gül University,
Kayseri 38080, Turkey
e-mail: burak.bal@agu.edu.tr

M. Koyama
Department of Mechanical Engineering,
Kyushu University,
Nishi-ku 819-0395, Fukuoka, Japan

D. Canadinc
Department of Mechanical Engineering,
Advanced Materials Group (AMG);
Surface Science and
Technology Center (KUYTAM),
Koç University,
Sariyer,
Istanbul 34450, Turkey

G. Gerstein
Institut für Werkstoffkunde (Materials Science),
Leibniz Universität Hannover,
An der Universität 2,
Garbsen 30823, Germany

H. J. Maier
Institut für Werkstoffkunde (Materials Science),
Leibniz Universität Hannover,
An der Universität 2,
Garbsen 30823, Germany

K. Tsuzaki
Department of Mechanical Engineering,
Kyushu University,
Nishi-ku 819-0395, Fukuoka, Japan

On the Utility of Crystal Plasticity Modeling to Uncover the Individual Roles of Microdeformation Mechanisms on the Work Hardening Response of Fe-23Mn-0.5C TWIP Steel in the Presence of Hydrogen

This paper presents a combined experimental and theoretical analysis focusing on the individual roles of microdeformation mechanisms that are simultaneously active during the deformation of twinning-induced plasticity (TWIP) steels in the presence of hydrogen. Deformation responses of hydrogen-free and hydrogen-charged TWIP steels were examined with the aid of thorough electron microscopy. Specifically, hydrogen charging promoted twinning over slip–twin interactions and reduced ductility. Based on the experimental findings, a mechanism-based microscale fracture model was proposed, and incorporated into a visco-plastic self-consistent (VPSC) model to account for the stress–strain response in the presence of hydrogen. In addition, slip-twin and slip–grain boundary interactions in TWIP steels were also incorporated into VPSC, in order to capture the deformation response of the material in the presence of hydrogen. The simulation results not only verify the success of the proposed hydrogen embrittlement (HE) mechanism for TWIP steels, but also open a venue for the utility of these superior materials in the presence of hydrogen. [DOI: 10.1115/1.4038801]

Keywords: hydrogen embrittlement, crystal plasticity, TWIP steel, strain hardening, microstructure

1 Introduction

With the rapid developments in different types of modern engineering applications, such as in the automotive, defense, and mining industries, austenitic Fe-Mn-C twinning-induced plasticity (TWIP) steels have increasingly attracted attention due to their exceptional mechanical properties, including high work hardening capacity and high tensile strength with significant ductility [1–3]. TWIP steels have been subject to several studies [4–6], many of which indicate that these superior mechanical properties arise from the presence of deformation twins (TWIP effect) and the occurrence of dynamic strain aging [7–10]. The most important factor affecting the TWIP effect is the stacking fault energy (SFE). Specifically, as the SFE decreases, the level of energy required for the abrupt lattice rotation associated with mechanical twinning also decreases, which enhances twin formation. In TWIP steels, due to their low or medium SFE values ranging from 12–40 mJ/m^2 [11,12], twin nucleation starts at the onset of plastic deformation and the volume fractions of micro and nanotwins increase concomitant with plastic strain, forming $\Sigma 3$ twin boundaries, which reduce the mean free path of dislocations and act as strong obstacles against dislocation motion, eventually providing high work hardening capacity [13,14]. In addition, dynamic strain aging, facilitated by the reorientations of carbon members of the C–Mn couples in the cores of dislocations, which causes serrated flow by small strain localizations and delays necking [15]. Thereby, TWIP steels, which have face-centered cubic crystal structure at room temperature, possess excellent elongation to fracture (up to 90%) and high tensile strength (up to 1500 MPa), in addition to relatively lower density ($\rho \approx 7.3$ g/cm^3) and significantly higher energy-absorption capacity (0.5 J/mm^3) as compared to conventional steels [16–19].

Despite these superior mechanical properties, it has been also reported that TWIP steels are vulnerable to hydrogen embrittlement (HE), which serves as a degradation mechanism and causes unexpected sudden failure in metallic materials [20–23]. Therefore, understanding both the HE susceptibility and the active hardening mechanisms in TWIP steel is of utmost importance for the utilization of TWIP steels in the automotive industry and for hydrogen-based energy applications. Previous works on the subject matter have mostly focused on the effects of hydrogen on the

[1]Corresponding author.

Contributed by the Materials Division of ASME for publication in the Journal of Engineering Materials and Technology. Manuscript received June 1, 2017; final manuscript received December 11, 2017; published online February 8, 2018. Assoc. Editor: Said Ahzi.

macroscopic response of TWIP steel [24,25], and effects of alloying elements [25–27], grain size [28,29], and hydrogen content [21] on the HE susceptibility of TWIP steels. Moreover, deformation response of TWIP steel was investigated with a focus of microscale deformation mechanisms [3,4].

However, the number and scope of studies focusing on both the investigation of hydrogen effects and the different hardening mechanisms in high-Mn austenitic steels have been very limited. Detailed investigations on these aspects have previously been carried out on Hadfield steel, which can be considered as a precursor material to TWIP steels [30–32]. For instance, the role of dense dislocation walls and grain boundary misorientation angle (GBMA) on the deformation response of Hadfield steel was investigated and a general formulation accounting for the effects of these mechanisms on material response was established [30,31]. Furthermore, length scales associated with twin lamellae spacing and grain boundaries in Hadfield steel were successfully incorporated into crystal plasticity simulations [32]. All these works on Hadfield steel constitute an initial step for the crystal plasticity modeling of the deformation response of TWIP steel, which exhibits a similar and equally complicated microstructure evolution under plastic deformation.

The contribution of twinning to the overall hardening is especially important in TWIP steels, which was previously investigated by utilizing a crystal plasticity based finite element method [33]. Furthermore, an analytical model was proposed to identify the effects of dislocations, twin boundaries, and grain boundaries on the deformation response of TWIP steel [34]. However, the influence of interstitial hydrogen on the material response of polycrystalline TWIP steel is generally ignored in the conventional crystal plasticity models. In addition, to the best of the authors' knowledge, no crystal plasticity model that takes into account both slip–twin and slip–grain boundary interactions, and hydrogen effects on the stress–strain response of TWIP steel has been forwarded yet, which constituted the major motivation for undertaking the current work.

In the present study, the roles of the different hardening mechanisms on the overall material response of Fe-23Mn-0.5C TWIP steel were quantified. For this purpose, a unique crystal plasticity approach was developed, which takes into account the individual contributions of slip–grain boundary and slip–twin interactions in the presence of hydrogen to the overall hardening. Specifically, a physically based constitutive equation was derived by modifying the well-known classical Voce hardening rule, and implemented into the visco-plastic self-consistent (VPSC) model. The modeling results, which demonstrate the individual influences of different hardening mechanism on the deformation response of TWIP steel, were compared to the experimental results obtained from tensile tests on the hydrogen-free and hydrogen-charged specimens at a moderate strain rate and room temperature. The simulation results not only demonstrated the success of the proposed model in predicting the stress–strain response of TWIP steel in the presence of hydrogen, but also shed light onto the complicated interactions of microdeformation mechanisms and the effect on solute hydrogen on the strain hardening response of TWIP steel. Overall, the findings of the combined experimental and theoretical study presented herein open a new venue for the utility of TWIP steels in applications operating in demanding environments, such as hydrogen storage.

2 Experimental Procedures and Results

In the present study, a TWIP steel was investigated, and its chemical composition is presented in Table 1. The steel was solution treated at 1273 K for 1 h, and samples were extracted from the bulk material by electro discharge machining. The average grain size of the samples was 23 μm including the annealing twin boundaries. Following electro discharge machining, half of the specimens were charged with hydrogen, whereas the others were not exposed to hydrogen gas for the sake of clearly demonstrating the role of HE. The hydrogen gas used in charging the samples was high purity (99.999%), and the specimens were exposed to the hydrogen gas atmosphere under a pressure of 7.3 MPa at 423 K for one week. The hydrogen desorption behavior was analyzed by thermal desorption spectroscopy between room temperature and 873 K at a heating rate of 400 K/h. The cumulative diffusible hydrogen content of the samples was measured as 5.58 wt ppm.

Table 1 Chemical composition of the TWIP steel studied in this work (in wt %)

C	Si	Mn	Si	P	S	Fe
0.51	0.27	22.6	0.27	<0.001	0.0072	Balance

Uniaxial monotonic tensile deformation tests were conducted on the specimens with and without hydrogen precharging at initial strain rates of 0.6×10^{-3} and 0.6×10^{-4} s^{-1} at ambient temperature. These strain rates are sufficiently low to allow hydrogen to interact with dislocations [35]. Complimentary microstructural observations were conducted with the aid of scanning electron microscopy (SEM), transmission electron microscopy (TEM), and electron backscatter diffraction (EBSD) measurements in order to examine the fracture surface characteristics and microstructural features, such as dislocations and twins. Furthermore, deformation-induced surface topography was observed by SEM in specimens tested at a strain rate of 0.6×10^{-4} s^{-1}. For TEM work, thin foils were extracted from the samples in the form of flat disks with a thickness of 400 μm. These disks were then mechanically thinned down to 80 μm, and electropolished on both sides by conventional twin-jet electropolishing with an electrolyte consisting of 80 ml 60% perchloric acid, 500 ml butoxyethanol, and 420 ml 100% acetic acid, in order to obtain large electron-transparent areas. The electropolishing was conducted at −12 °C under an acceleration voltage of 22.5 V. The EBSD analysis was carried out under a voltage of 20 kV and with a beam step size of 200 nm.

The true stress–true strain curves along with the specimen dimensions for tensile testing are given in Fig. 1. Clearly HE is more pronounced at the low strain rate. In a related study, we proposed a five-step microscale fracture process in the presence of HE, which is schematically described in Fig. 2 [36]. Specifically, glide dislocations (or slip lines) and secondary twins distort the primary twin boundaries (1–2), and generate potential trap sites for hydrogen (3). With the formation of nanotwins inside the initially formed primary twins and the occurrence of slip dislocation pile ups (4), microstructural stress concentration on the primary twin boundaries increases. Once the stress concentration cannot be accommodated plastically due to the reduction in cohesive energy resulting from trapped hydrogen, twin boundary cracking takes place (5). These effects were all taken into account by the crystal plasticity model presented herein.

The microscopy results obtained from the specimen deformed to 30% strain at 0.6×10^{-4} s^{-1} without hydrogen charging is shown in Fig. 3. The corresponding rolling direction inverse pole figure map is shown in Fig. 3(*a*), where the horizontal arrow represents the actual tensile direction. Accordingly, a relatively large volume of deformation twins was observed particularly along the ⟨111⟩ orientation. In addition, the corresponding TEM result (Fig. 3(*b*)) demonstrated that slip, two different twin variants, nanotwin formation and slip–twin boundary interaction were simultaneously

Table 2 Experimentally-based hardening parameters and constants used in the proposed crystal plasticity model

K	A	μ (GPa)	b (m)	d (m)
8×10^4	0.4	71	2.58×10^{-10}	23×10^{-6}
t_1 (nm) H free	t_2 (nm) H induced	V_H (m^3 mol^{-1})	v	N_A (mol^{-1})
35	25	2×10^{-6}	0.24	6.022×10^{23}

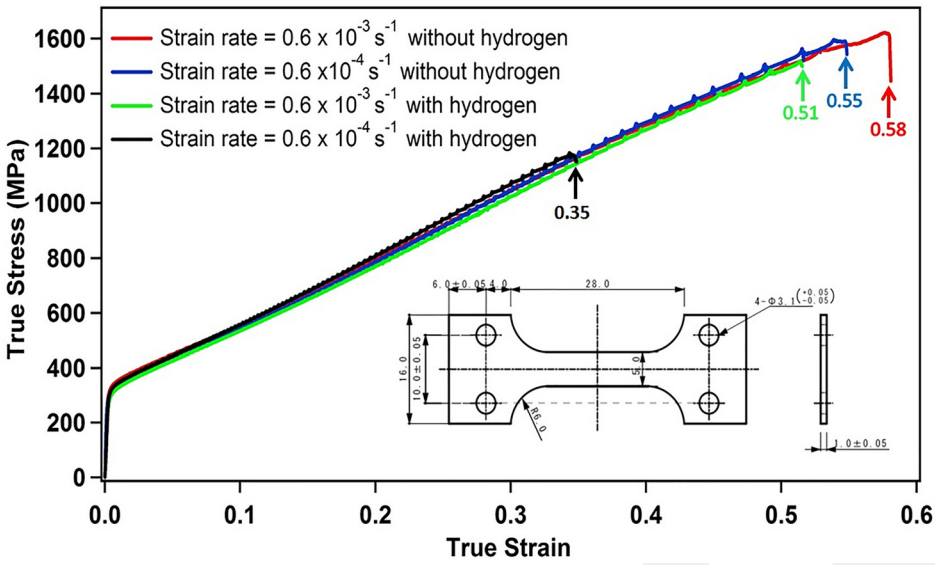

Fig. 1 Tensile response of the Fe-23Mn-0.5C TWIP steels with and without hydrogen charging at different strain rates. Data recompiled from Ref. [36].

present. The simultaneous activities of multiple microdeformation mechanisms were also evidenced by the GBMA distribution, where the volume fraction of high-angle grain boundaries induced by plastic deformation dominated (Fig. 3(*c*)), and the intense surface relief that was apparent in the SEM (Fig. 3(*d*)).

The microstructure evolution of the specimen deformed with identical deformation parameters but following hydrogen charging is presented in Fig. 4. The rolling direction-inverse pole figure map shows the formation of twin bundles, Fig. 4(*a*). The corresponding TEM analysis demonstrated an excessive slip activity and slip–grain boundary interactions, Fig. 4(*b*). Even though the corresponding GBMA distribution (Fig. 4(*c*)) and the surface relief (Fig. 4(*d*)) were similar to those of the hydrogen-free sample (Figs. 3(*c*) and 3(*d*)), enhanced slip activity as evidenced by slip bands, and twins and voids were coexistent upon deformation in the presence of hydrogen.

When the strain rate was increased tenfold to 0.6×10^{-3} s^{-1}, the hydrogen-free sample deformed to 30% strain exhibited a significant volume of twin bundles (Fig. 5(*a*)), similar to the hydrogen-charged sample deformed at 0.6×10^{-4} s^{-1} (Fig. 4(*a*)). However, in the case of the hydrogen-free sample deformed at 0.6×10^{-3} s^{-1}, high density dislocation wall (HDDW) formation was also evident, which constitutes an additional barrier against dislocation glide (Fig. 5(*b*)). Despite the one order of magnitude increase in strain rate, the corresponding GBMA distribution (Fig. 5(*c*)) does not significantly differ from that of the hydrogen-free sample deformed at the slower strain rate (Fig. 3(*c*)). However, both slip (Fig. 5(*b*)) and twin and nanotwin (Fig. 5(*d*)) activity are more prominent, further promoting slip–twin interactions, which is expected due to the increased strain rate in this class of materials [3,4,30]. As for the hydrogen-charged specimen deformed to 30% strain at 0.6×10^{-3} s^{-1}, it is evident that hydrogen enhanced the volume fraction of twin bundles (Fig. 6(*a*)), and promoted the formation of two different twin variants over slip–twin interactions, accompanied by nanotwin formation within primary twins (Fig. 6(*b*)). The corresponding GBMA distribution (Fig. 6(*c*)) remained similar to those of the other three samples (Figs. 3(*c*), 4(*c*) and 5(*c*)), exhibiting a larger volume fraction of high-angle grain boundaries, mainly due to the relatively larger plastic deformation of 30%. Furthermore, HDDW formation can be observed in Fig. 6(*d*).

Scanning electron microscopy fracture micrographs of hydrogen-free specimens strained at 0.6×10^{-4} s^{-1} and 0.6×10^{-3} s^{-1} are presented in Figs. 7(*a*) and 7(*b*), respectively. While the dimples evidence a dominantly ductile fracture on these surfaces, the fracture surfaces of hydrogen-charged specimen deformed at 0.6×10^{-4} s^{-1} and 0.6×10^{-3} s^{-1} feature cleavage facets, as shown in Figs. 7(*c*) and 7(*d*), respectively, which implies that the fracture mode turned into quasi-cleavage upon charging with hydrogen. Cleavage facets were more obvious at the low strain rate (Fig. 7(*c*)) when compared to the higher strain rate (Fig. 7(*d*)). Combination of different morphologies, including cleavage facets and microvoid coalescence, were observed on the fracture surface of sample deformed at the higher strain rate (Fig. 7(*d*)). Thus, one can conclude that HE was more pronounced at the lower strain rate since more time was allocated for hydrogen to interact with dislocations and twins, supporting the proposed HE mechanism schematically described in Fig. 2.

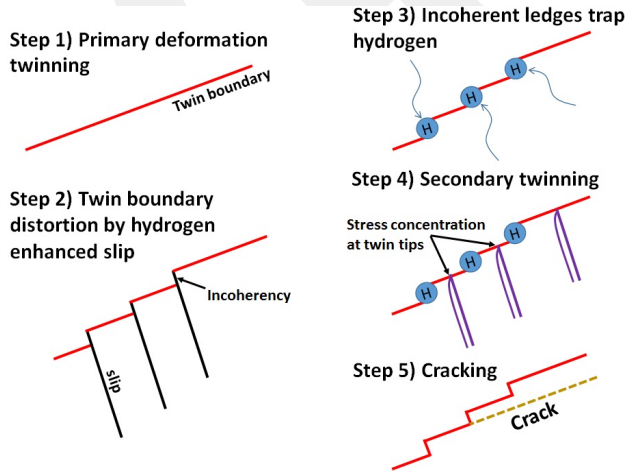

Fig. 2 Schematic representation of the proposed five-step microscale fracture process in the presence of hydrogen

3 Theory and Calculations

Based on the experimental findings presented in Sec. 2, the total hardening is attributed to four factors in the model proposed, namely, forest dislocation hardening, slip–twin interactions, GBMA-dependent slip–grain boundary interactions and the effect

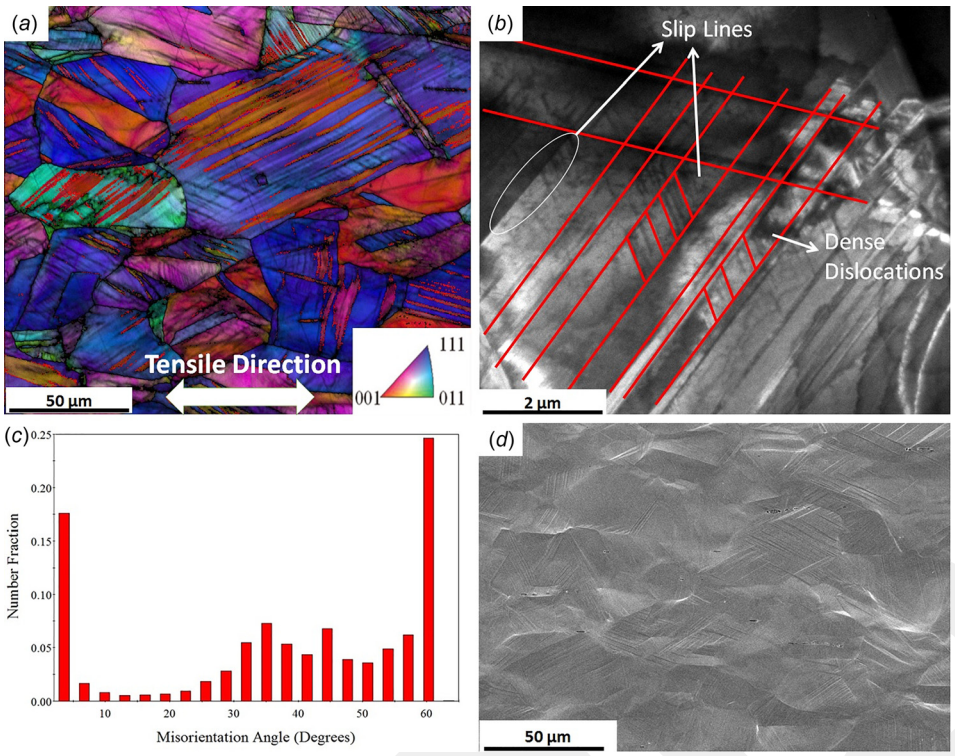

Fig. 3 Microstructure of hydrogen-free specimen deformed to 30% at 0.6×10^{-4} s^{-1}: (*a*) EBSD micrograph and orientation map, (*b*) TEM micrograph, (*c*) GBMA distribution map, and (*d*) in situ SEM micrograph of the surface

of hydrogen. In order to include these hardening contributions, and the roles of texture and the corresponding anisotropy, a VPSC crystal plasticity model [37], which is capable of capturing the deformation characteristics of the material at the slip system level, was modified. The remainder of this section details the corresponding modifications made to VPSC in order to properly treat all the aforementioned hardening mechanisms within a single strain hardening formulation.

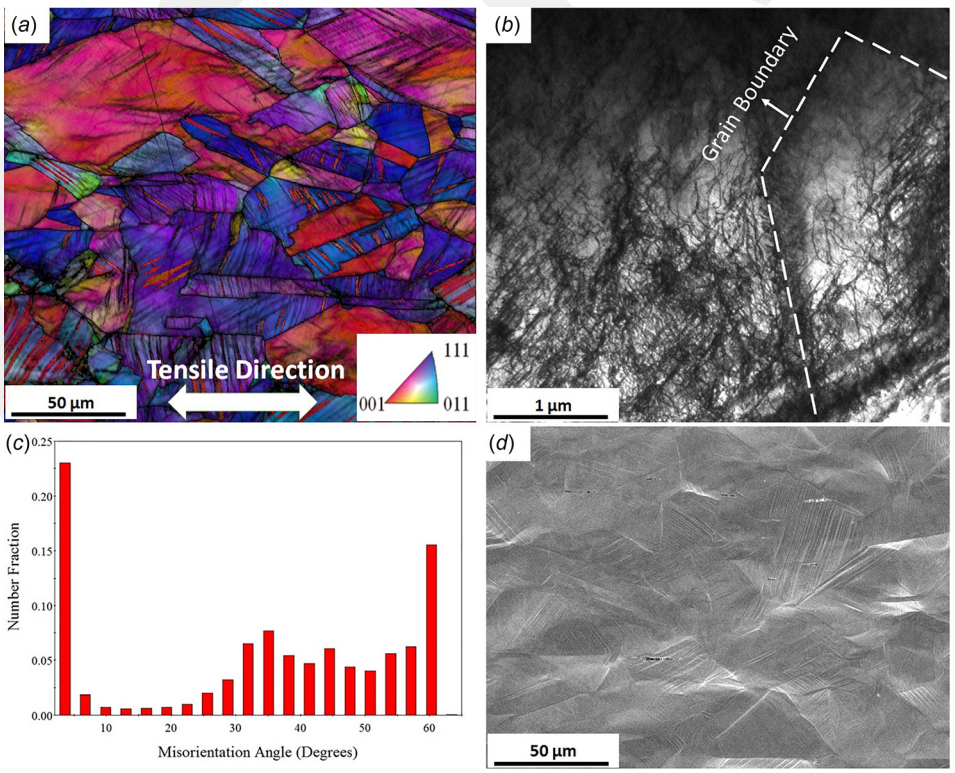

Fig. 4 Microstructure of hydrogen-charged specimen deformed to 30% at 0.6×10^{-4} s^{-1}: (*a*) EBSD micrograph and orientation map, (*b*) TEM micrograph, (*c*) GBMA distribution map, and (*d*) the in situ SEM micrograph of the surface

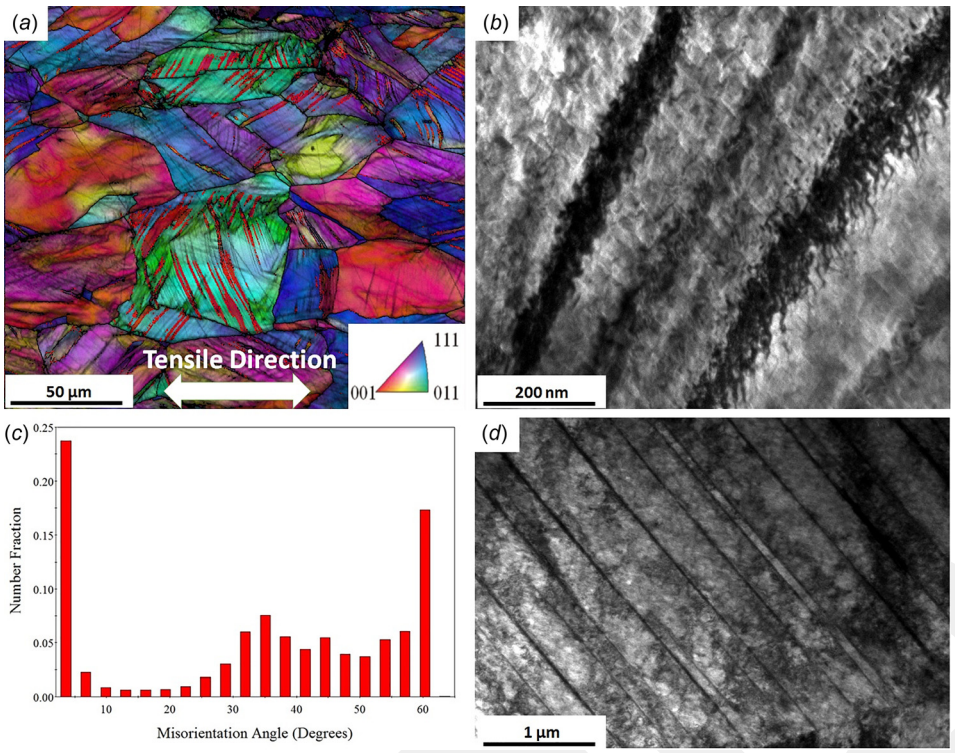

Fig. 5 Microstructure of hydrogen-free specimen deformed to 30% at 0.6×10^{-3} s^{-1}: (*a*) EBSD micrograph and orientation map, (*b*) TEM micrograph showing HDDWs, (*c*) GBMA distribution map, and (*d*) TEM micrograph demonstrating the presence of nanotwins

3.1 Incorporating the Roles of Slip–Twin and GBMA-Dependent Slip-Grain Boundary Interactions Into VPSC. In order to better understand the effect of slip–twin interactions on the strain hardening response of the Fe-23Mn-0.5C TWIP steel, the contribution of slip–twin interactions was incorporated into the VPSC model as an additional mechanism which affects the material response. Specifically, both twin boundaries and grain boundaries act as obstacles to dislocation motion as evidenced

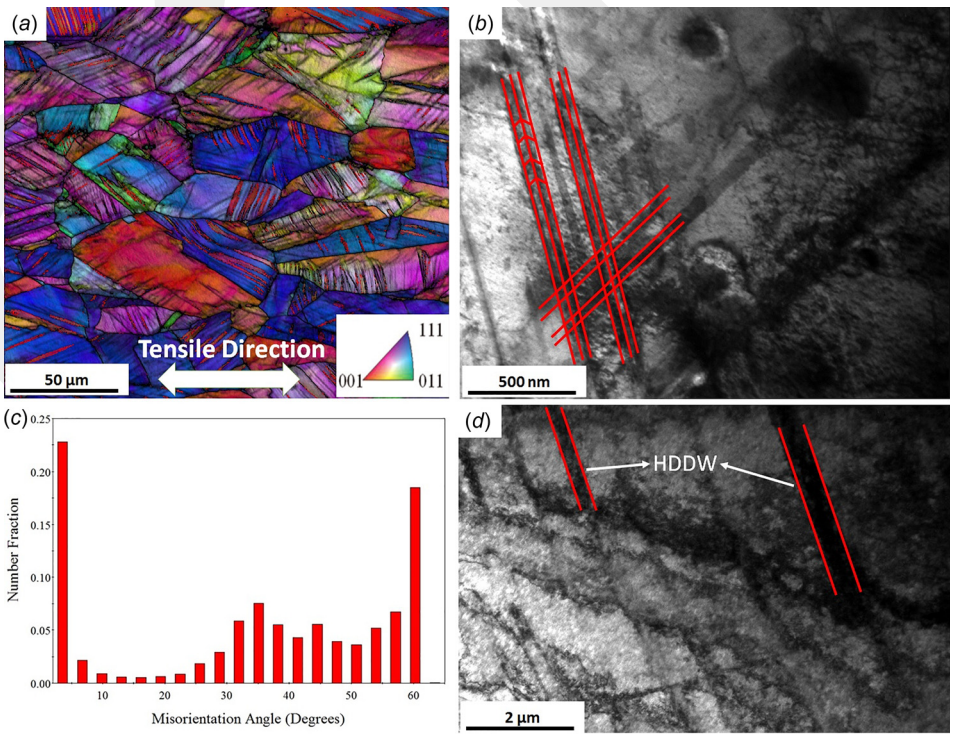

Fig. 6 Microstructure of hydrogen-charged specimen deformed to 30% at 0.6×10^{-3} s^{-1}: (*a*) EBSD micrograph and orientation map, (*b*) TEM micrograph showing interactions with nanotwins, (*c*) GBMA distribution map, and (*d*) TEM micrograph with HDDWs

from TEM observations, and an increase in the twin volume fraction decreases the mean free path of dislocations. Thus, the rate of overall dislocation density was considered in the form of

$$\dot{\rho} = \sum_n \{k_1\sqrt{\rho} - k_2\rho\}|\dot{\gamma}^n| + \sum_n \sum_r \frac{K}{cb}\cos\theta_{nr}|\dot{\gamma}^n| + \sum_n \sum_q \frac{K}{db}(1+\sin\theta_q)|\dot{\gamma}^n| \quad (1)$$

where b represents the Burgers vector, k_1 and k_2 are constants that define the athermal (statistical) storage of the glide dislocations and dynamic recovery in the domains outside the HDDWs, respectively [38]. K is a geometric constant and the terms $\sum_n\sum_r \frac{K}{cb}\cos\theta_{nr}|\dot{\gamma}^n|$ and $\sum_n\sum_q \frac{K}{db}(1+\sin\theta_q)|\dot{\gamma}^n|$ account for the contributions due to the interaction between the dislocations on the active slip system n and the active twin system r; and the interaction between the dislocations on the active slip system n, and the boundary between the grain in consideration and its qth neighbor, respectively [30,31,39,40] (Fig. 8). The angle θ_{nr} is the angle between the plane normal of the active slip system and the plane normal of the active twinning system (Fig. 8(*b*)), and was incorporated as a measure of the role of slip–twin interactions in a geometric sense. Moreover, the angle θ_q is the misorientation angle between the surface normals of neighboring grains (Fig. 8(*a*)). These angles are variables and take different values during deformation depending on the active slip systems and reorientation in the lattice. As the GBMA increases, the role of slip–grain boundary interaction on the strain hardening response of the material would also increase due to the decreasing possibility of glide dislocations crossing the grain boundary with the neighboring grain [31]. For the small misorientation angles, the dislocations can cross the neighboring grain boundary upon increasing the applied stress, which decreases the contribution of slip–grain boundary interactions to the overall strain hardening response. In this formulation, the term c represents the average spacing between twins and d represents the average grain size of the aggregate.

The flow stress τ is defined in the traditional Taylor hardening format as

$$\tau - \tau_0 = \alpha\mu b\sqrt{\rho} \quad (2)$$

where α is the dislocation interaction parameter, μ is shear modulus, and τ_0 is a reference strength, which is taken as the microscopic yield in our analysis and calculated using the Taylor factor. Specifically, Taylor factors for both hydrogen-free and hydrogen-charged materials were determined after EBSD analysis and the macroscopic yield strength, which was calculated by the 0.2% offset method, was divided into the Taylor factor to determine microscopic yield. The relationship between the term c and the volume fraction of twins, f, is defined as follows:

$$\frac{1}{c} = \frac{1}{2t}\frac{f}{1-f} \quad (3)$$

where t represents the average twinned region thickness determined based on the TEM analysis (Table 2). The average twin thickness was measured as the distance between two twin boundaries and the volume fraction of twins was calculated using the default treatment in the VPSC algorithm [37]. In particular, the shear strain contributed by each twin system is tracked within each grain and divided by the characteristic twin shear to calculate the volume fraction of twins [37]. Specifically, it was set to the 0 before the deformation and updated based on accumulated twin volume fraction.

Upon taking the time derivative of the flow stress with constant reference strength, the rate of the flow stress is obtained as

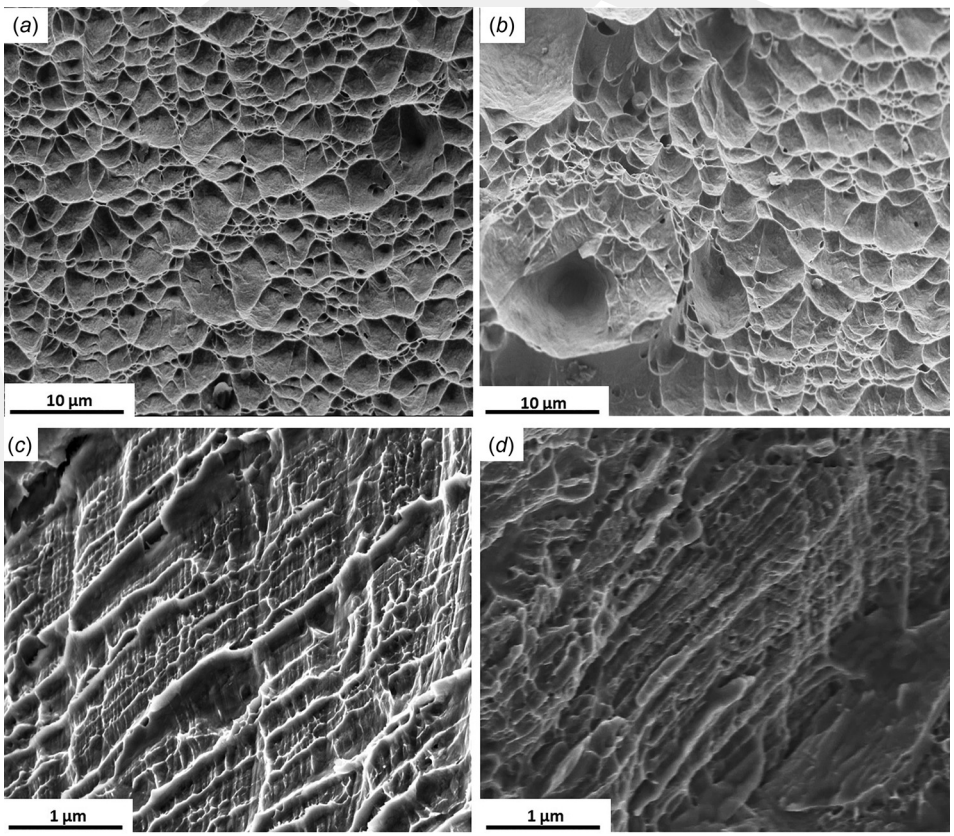

Fig. 7 Scanning electron microscopy surface fractographs of the (*a*) hydrogen-free specimen at 0.6×10^{-4} s^{-1} (*b*) hydrogen-free specimen at 0.6×10^{-3} s^{-1} (*c*) hydrogen-charged specimen at 0.6×10^{-4} s^{-1}, and (*d*) hydrogen-charged specimen at 0.6×10^{-3} s^{-1}

$$\dot{\tau} = \frac{\alpha\mu b\dot{\rho}}{2\sqrt{\rho}} \tag{4}$$

Substituting Eq. (1) into Eq. (4) results in

$$\dot{\tau} = \sum_n \left[\left\{ k_1 \frac{\alpha\mu b}{2} - k_2 \frac{\alpha\mu b\sqrt{\rho}}{2} \right\} + \frac{K\alpha\mu}{2c\sqrt{\rho}} \sum_r \cos\theta_{nr} + \frac{K\alpha\mu}{2d\sqrt{\rho}} \sum_q (1 + \sin\theta_q) \right] |\dot{\gamma}^n| \tag{5}$$

From Eq. (2), the following identity is obtained for the square root of the density of dislocations

$$\sqrt{\rho} = \frac{\tau - \tau_0}{\alpha\mu b} \tag{6}$$

Once Eqs. (3) and (6) are substituted into Eq. (5), the rate of flow stress evolution is given by

$$\dot{\tau} = \sum_n \left[\left\{ k_1 \frac{\alpha\mu b}{2} - k_2 \frac{\tau - \tau_0}{2} \right\} + \frac{K\alpha^2\mu^2 b}{4t(\tau - \tau_0)} \frac{f}{1-f} \sum_r \cos\theta_{nr} + \frac{K\alpha^2\mu^2 b}{2d(\tau - \tau_0)} \sum_q (1 + \sin\theta_q) \right] |\dot{\gamma}^n| \tag{7}$$

One should note that the term $\{k_1\alpha\mu b/2 - k_2\tau - \tau_0/2\}$ in Eq. (7) is the linear Voce hardening term (Eq. (9)). Having noted this, Eq. (7) can also be written as

$$\dot{\tau} = \sum_n \left[\left\{ \theta_0 \left(\frac{\tau_s - \tau}{\tau_s - \tau_0} \right) \right\} + \frac{K\alpha^2\mu^2 b}{4t(\tau - \tau_0)} \frac{f}{1-f} \sum_r \cos\theta_{nr} + \frac{K\alpha^2\mu^2 b}{2d(\tau - \tau_0)} \sum_q (1 + \sin\theta_q) \right] |\dot{\gamma}^n| \tag{8}$$

where θ_0 is the constant strain hardening rate, and τ_s represents the saturation stress in the absence of geometric effects, or the threshold stress. The hardening is defined by an extended Voce law [41], which is characterized by the evolution of the threshold stress (τ^s) with accumulated shear strain (Γ) in each grain of the form

$$\tau^s = \tau_0 + (\tau_1 + \theta_1\Gamma)\left(1 - \exp\left(-\frac{\theta_0\Gamma}{\tau_1}\right)\right) \tag{9}$$

where τ_0 is the reference strength, and τ_1, θ_0, and θ_1 are the parameters that define the hardening behavior [41]. The hardening law defined by Eq. (9) characterizes the onset of plasticity and the saturation of threshold stress at larger strains.

3.2 Modeling the Role of Hydrogen Embrittlement on Strain Hardening. In order to incorporate the effect of hydrogen on the material response of the Fe-23Mn-0.5C TWIP steel and to observe the consequences of hydrogen-induced softening at the microscale on the macroscopic response of material, the presence of hydrogen was incorporated into Eq. (8) as an additional mechanism affecting the strain hardening. Specifically, the influence of hydrogen was modeled by a continuous distribution of dilatation lines whose strength depends on the local solvent concentration around arrested edge dislocations. To begin with, the shear stress imposed on a positive edge dislocation due to hydrogen atom concentration is given by [42]

$$\tau_H = -\frac{\mu}{2\pi(1-\vartheta)} \frac{V_H}{N_A} \int_0^{2\pi} \int_{r_i}^{r_0} C(r,\emptyset) \frac{\sin 2\emptyset}{r} dr d\emptyset \tag{10}$$

where μ is shear modulus, V_H is the partial molar volume of hydrogen in solution, ϑ is Poisson's ratio, and N_A is the Avogadro number. The inner and outer cut-off radii of the hydrogen atmosphere surrounding the edge dislocation are given by r_i and r_o, respectively.

The time-dependent solute hydrogen concentration during deformation can be expressed as [43–45]

$$C(t_a) = C_m \left\{ 1 - \exp\left[-\left(\frac{C_0}{C_m} \right) (KDt_a)^n \right] \right. \tag{11}$$

where t_a is the effective time that the mobile dislocations have been arrested for, C_m is the saturation value of the solute concentration along the dislocation line, C_0 is the alloy solute concentration, and the term KD is the inverse of the characteristic solute diffusion time such that $t_d = (KD)^{-1}$. Specifically, the term D is the solute diffusion coefficient and K is the constant, which includes the solute-dislocation binding energy. The parameter n was taken as 2/3 [45,46].

At steady-state, the aging time is equal to the waiting time, where the latter is the average time the dislocations stay arrested at obstacles throughout the matrix; however, in order to determine the transient behavior of solute hydrogen concentration at nonsteady-state conditions, the aging time is assumed to evolve with the strain rate according to [45,47,48]

$$\frac{dt_a}{dt} = 1 - \frac{t_a}{t_w} \tag{12}$$

During deformation, mobile dislocations are pinned for an average waiting time, and then they glide until they come across the

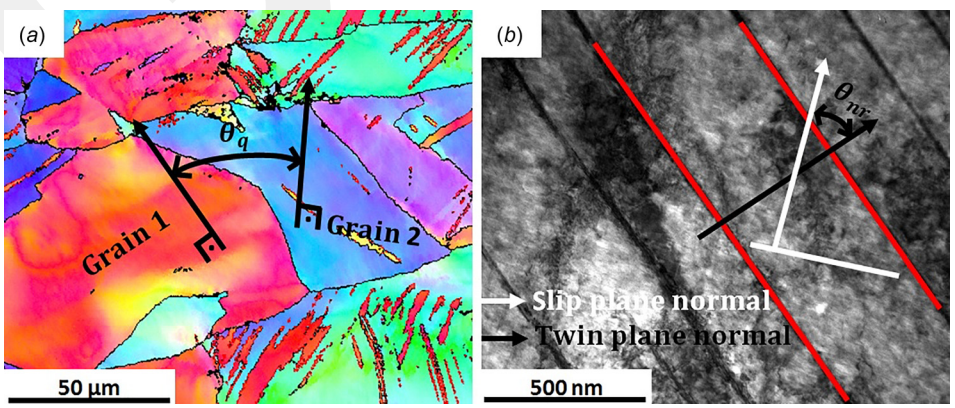

Fig. 8 Schematic representation of (*a*) misorientation angle between the surface normals of neighboring grains and (*b*) angle between the plane normal of the active slip system and the plane normal of the active twinning system

next pinning configuration. For steady-state conditions, the average waiting time can be calculated by the well-known Orowan equation, such that $t_w = \rho_m bL/\dot{\varepsilon}$, where ρ_m is moving dislocation density, L is the mean free path of the dislocations and $\dot{\varepsilon}$ is the strain rate. By contrast, the average waiting time for nonsteady-state conditions is a function of fundamental attempt frequency, ϑ_0, which depends on the moving dislocation density, Burgers vector, the Debye frequency, and the effective resolved shear stress-dependent energy barrier model, τ_{eff} [45,49–51]. Specifically, the average waiting time is expressed as

$$t_w = e^{\Delta E(\tau^n_{\text{eff}})/kT}/\vartheta_0 \tag{13}$$

For the calculation of the waiting time, the correct modeling of the energy barrier is very critical. Out of several energy barrier model formulations with different kinds of obstacles [44,52,53], the stress-dependent energy barrier model proposed by Kocks et al. was adopted in the current VPSC model

$$\Delta E(\tau^n_{\text{eff}}) = E_0\left[1 - \left(\frac{\tau^n_{\text{eff}}}{s^\alpha_{t0}}\right)^p\right]^q \tag{14}$$

In Eq. (14), E_0 is the zero effective shear stress activation energy, p and q represent the profiling parameters, and the constant s_{t0} stands for the thermal slip resistance at 0 K (Peierls stress), which is assumed to be equal to the same initial value for all slip systems. In this study, taking $p = 1$/s and $q = 3/2$ is considered to be adequately accurate for all systems [54]. Furthermore, the effective resolved shear stress on the slip system n is the difference between the resolved external stress, τ, and the resolved back stress representing the slip system resistance, s^n_a [50,51,55]

$$\tau^n_{\text{eff}} = |\tau^n| - s^n_a \tag{15}$$

The details of the effective resolved shear stress calculation and corresponding energy barrier model can be found in Ref. [48]. Once the energy barrier model is included and, the contribution of hydrogen is also accounted for, the hardening scheme of the crystal plasticity model (Eq. (8)) becomes

$$\dot{\tau} = \sum_n \left[\left\{\theta_0\left(\frac{\tau_s - \tau}{\tau_s - \tau_0}\right)\right\} + \frac{K\alpha^2\mu^2 b}{4t(\tau - \tau_0)}\frac{f}{1-f}\sum_r \cos\theta_{nr} + \frac{K\alpha^2\mu^2 b}{2d(\tau - \tau_0)}\sum_q (1 + \sin\theta_q)\right]|\dot{\gamma}^n| + S\frac{d\tau_H}{dt} \tag{16}$$

where S is the scaling factor that reflects the contribution of hydrogen to the overall hardening response throughout the whole grain. After substitution of Eqs. (11) and (12) into Eq. (10) for $n = 2/3$, and taking the time derivative of the shear stress imposed on a positive edge dislocation due to hydrogen, one obtains

$$\frac{d\tau_H}{dt} = -\frac{\mu}{2\pi(1-\nu)}\frac{V_H}{N_A}\int_0^{2\pi}\int_{r_i}^{r_o} \times \frac{2C_0[K(r,\text{Ø})D]^{\frac{2}{3}}\exp\left[-\left(\frac{C_0}{C_m}\right)(K(r,\text{Ø})Dt_a)^{\frac{2}{3}}\right]}{3t_a^{\frac{1}{3}}} \times \left(1 - \frac{t_a}{t_w}\right)\frac{\sin 2\text{Ø}}{r}drd\text{Ø} \tag{17}$$

It should be noted that elastic continuum theory is not applicable at the core of the dislocation, and thus, $r_i = b$ and $r_o = 10b$ are assigned as the integration limits for Eq. (17).

Finally, the modified hardening formulation used in the crystal plasticity computations, which includes the effects of slip–twin interactions, slip–grain boundary interactions, and HE on the strain hardening response of TWIP steel, can be expressed after substituting Eq. (17) into Eq. (16) as

$$\dot{\tau} = \sum_n \left[\left\{\theta_0\left(\frac{\tau_s - \tau}{\tau_s - \tau_0}\right)\right\} + \frac{K\alpha^2\mu^2 b}{4t(\tau - \tau_0)}\frac{f}{1-f}\sum_r \cos\theta_{nr} + \frac{K\alpha^2\mu^2 b}{2d(\tau - \tau_0)}\sum_q (1 + \sin\theta_q)\right]|\dot{\gamma}^n| - S\frac{\mu}{2\pi(1-\nu)}\frac{V_H}{N_A}\int_0^{2\pi}\int_{r_i}^{r_o} \times \frac{2C_0[K(r,\text{Ø})D]^{\frac{2}{3}}\exp\left[-\left(\frac{C_0}{C_m}\right)(K(r,\text{Ø})Dt_a)^{\frac{2}{3}}\right]}{3t_a^{\frac{1}{3}}} \times \left(1 - \frac{t_a}{t_w}\right)\frac{\sin 2\text{Ø}}{r}drd\text{Ø} \tag{18}$$

3.3 Simulation Results and Discussion. Schematic representations of the misorientation angle between the surface normals of neighboring grains, θ_q, and the angle between the plane normal of the active slip system and the plane normal of the active twinning system, θ_{nr}, are given in Fig. 8. In addition, a schematic representation of the employed approach in the proposed crystal plasticity model, which can quantify the contributions of different hardening mechanisms on the deformation response of TWIP steel, is shown in Fig. 9. Specifically, the VPSC algorithm based on Eqs. (1)–(9) was utilized to predict the macroscopic deformation response of hydrogen-free TWIP steel, which is triggered by several hardening mechanisms. The VPSC algorithm only considers plastic deformation that occurs when one or more slip or twinning systems become active up to the tensile strength of a material. Thus, the crystal plasticity simulations were carried out considering only the plastic deformation regime, which is a valid approach since the elastic response of TWIP steel is not rate dependent. During the crystal plasticity simulations, experimentally measured texture, crystal structure, and number of grains of the material were utilized as direct input, and 12 primary slip, as well as 12 primary and secondary twinning systems were activated. The classical Voce type hardening rule was extended to include the stress concentration resulting from the slip–twin and slip–grain boundary interactions based on Eqs. (1)–(9). After calibrating the Voce hardening parameters, which were determined by a step-by-step procedure based on a secant type of inclusion–matrix interaction, the individual roles of slip–twin and slip–grain boundary interactions were quantified by eliminating their contributions from the unique strain hardening model (Eq. (9)). Results of the corresponding VPSC simulations of hydrogen-free TWIP steels at $0.6 \times 10^{-3}\,\text{s}^{-1}$ and $0.6 \times 10^{-4}\,\text{s}^{-1}$ with their corresponding slip and twin hardening parameters are presented in Figs. 10 and 11, respectively: in both cases, the effect of slip–twin interactions is more significant than the effect of dislocation–grain boundary interactions on the strain hardening behavior of hydrogen-free TWIP steels. Furthermore, their effects on strain hardening become more prominent concomitant with the applied strain.

Once the model successfully predicted the deformation response of the hydrogen-free samples at two different strain rates, employing the calibrated slip and twin hardening parameters, the effect of HE on the strain hardening behavior of TWIP steel was modeled through Eqs. (10)–(18). VPSC simulations of hydrogen-charged TWIP steels at $0.6 \times 10^{-3}\,\text{s}^{-1}$ and $0.6 \times 10^{-4}\,\text{s}^{-1}$ are presented in Figs. 12 and 13, respectively. Specifically, Kocks-type stress-dependent energy barrier was modeled to calculate the corresponding waiting and the corresponding aging times, which were then used to model the time-dependent solute hydrogen concentration during deformation. Hydrogen-induced shear stress was calculated by integrating the hydrogen concentration over the dislocation region from $r_i = b$ and $r_o = 10b$ and $\text{Ø} = 0$ to $\text{Ø} = 2\pi$. The cylindrical coordinate system utilized to describe the location of a hydrogen atom with respect to the dislocation is shown in Fig. 9. The effect of hydrogen-induced shear stress rate was incorporated into the hardening rule considering the scaling factor based on Eq. (18).

The current formulation considers the interactions of slip–twin and dislocation–grain boundary on active slip systems, and HE, all as a hardening mechanism. The VPSC simulations were conducted utilizing the same slip and twin hardening parameters to follow the same hardening trend and observe the individual role of HE. In order to validate the model, simulation results were compared to the experimental deformation responses of the hydrogen-charged TWIP steels. The close prediction of the experimental response and modified VPSC model validates the proposed approach.

4 Final Remarks

The model presented in this paper incorporates multiple parameters that dictate the work hardening response of the TWIP steel, in addition to HE, however; not only the deformation response was successfully captured, but also the individual contributions of the active microdeformation mechanisms were clearly laid out with the aid of the theory proposed herein (Figs. 10–13). The success of identifying the individual roles of each mechanism, which constitutes a challenging experimental task, can be associated with the step-by-step approach followed (Fig. 9). An equally important reason is that the interaction formulations were proposed based on three-dimensional actual geometric interactions dictating the local stress concentrations (Fig. 8) such that the proposed model is both physically grounded and realistic in terms of incorporating the microdeformation mechanism interactions.

An important observation regarding the hydrogen effect is that hydrogen leads to a significant decrease in twin thickness and increase in twin plates, which promotes an increased frequency of slip–twin interactions within the matrix. This is also in good agreement with the numerical approach such that the rate of flow stress is inversely proportional to the twin thickness, and the enhanced slip–twin interactions can be observed more clearly at the lower strain rate. The average twin thicknesses for each case were experimentally determined based on numerous TEM images taken during this study: for the hydrogen-free samples, the

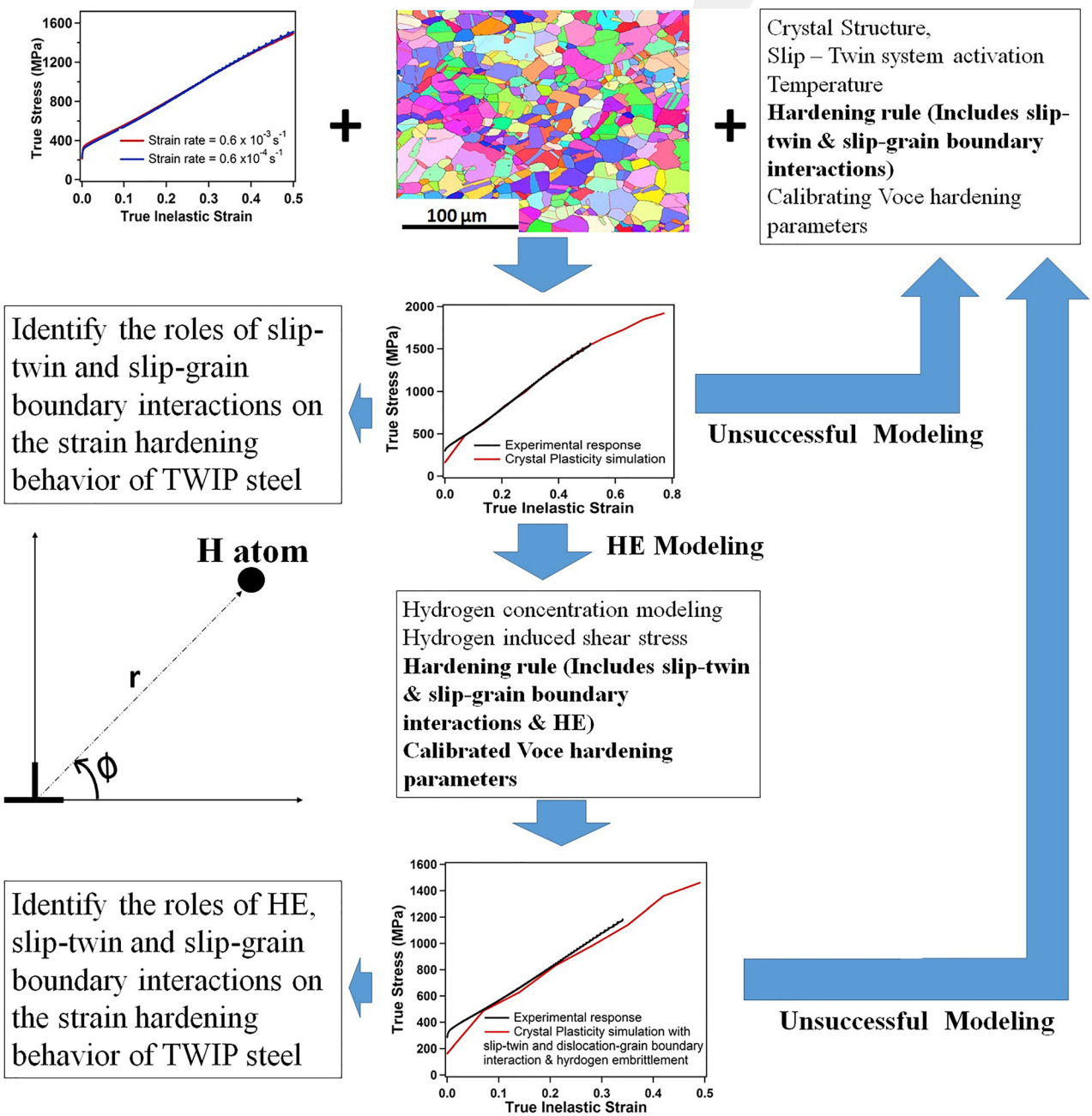

Fig. 9 Flowchart describing the approach adopted in the present crystal plasticity model

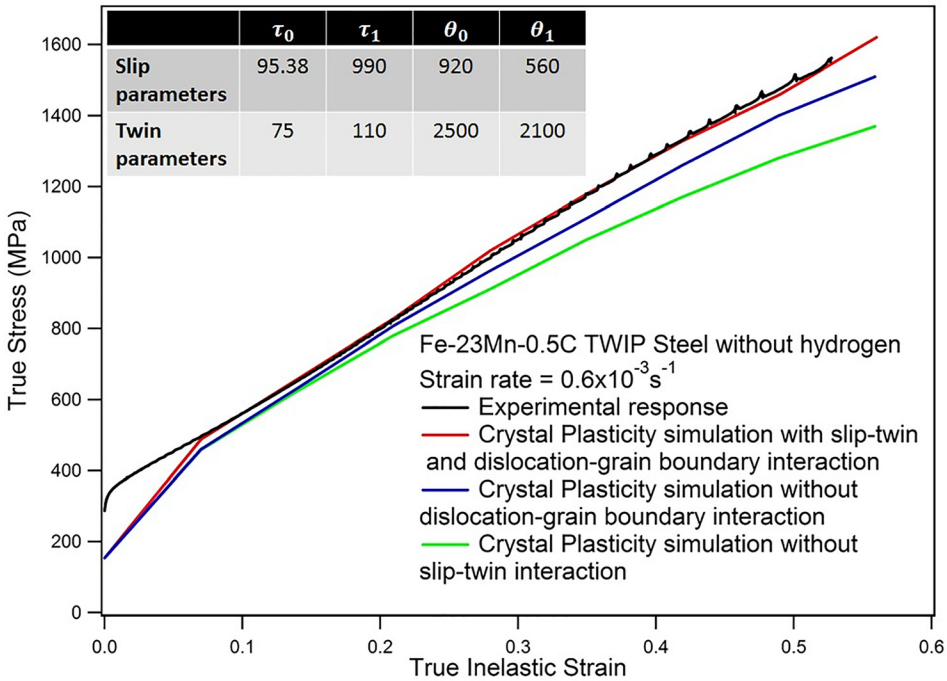

Fig. 10 Visco-plastic self-consistent simulations of the deformation response of Fe-23Mn-0.5C hydrogen-free TWIP steel at $0.6 \times 10^{-3}\ s^{-1}$

average twin thickness decreased from 150 nm to 35 nm when the strain rate changed from $0.6 \times 10^{-3}\ s^{-1}$ to $0.6 \times 10^{-4}\ s^{-1}$. The same decrease in the strain rate resulted in a decrease of the average twin thickness from 55 nm to 25 nm in the hydrogen-charged samples. Still, it should be noted that the volume of material examined by TEM is very small, and thus, the true bulk twin thicknesses might be somewhat different. However, the reported values were provided with the aim of demonstrating the trend rather than the actual values.

Another important point emphasized by the current modeling results is that the proposed new HE mechanism (Fig. 2) can be effectively incorporated into the modified crystal plasticity model. In particular, the formation of primary twin boundaries was allowed by activating the twin systems in VPSC. Then, twin boundaries were distorted by slip lines due the incorporation of slip–twin interaction into the crystal plasticity model. Further incorporation of HE into the crystal plasticity model also altered the mechanical response and caused serrations. Overall, the good agreement between the experimental and simulation results indicates that the proposed HE mechanism, which is based on experimental findings, is indeed applicable for realistic simulations of the actual material behavior.

Finally, it should be noted that another important outcome of the modeling effort presented herein is the success of the

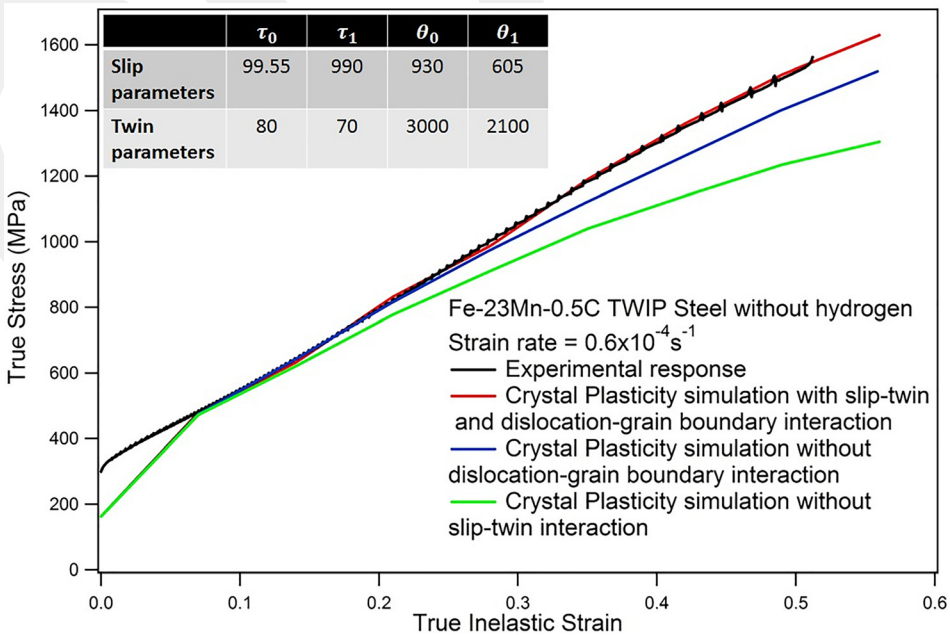

Fig. 11 Visco-plastic self-consistent simulations of the deformation response of Fe-23Mn-0.5C hydrogen-free TWIP steel at $0.6 \times 10^{-4}\ s^{-1}$

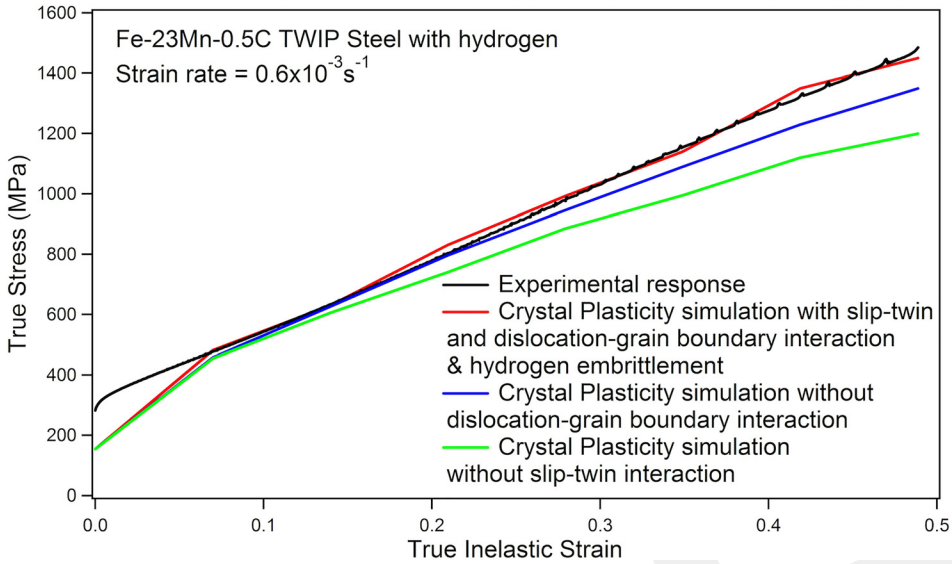

Fig. 12 Visco-plastic self-consistent simulations of the deformation response of Fe-23Mn-0.5C hydrogen-charged TWIP steel at 0.6×10^{-3} s^{-1}

incorporation of HE into the Voce hardening formulation. In fact, this phenomenon takes place by diffusion of hydrogen and its interactions with dislocations and twin boundaries, yet all interactions occur at the atomic level, making it impractical to experimentally observe. However, the formulation presented in this paper successfully incorporated the contribution of this atomic-level phenomenon to the overall work hardening response to the microlevel Voce hardening rule, which could be utilized in the modeling of other diffusion-based effects in metallic materials.

5 Conclusion

The combined experimental and theoretical analysis presented herein was undertaken with the aim of uncovering the individual roles of microdeformation mechanisms that are simultaneously active during the deformation of TWIP steels in the presence of hydrogen. In particular, deformation responses of hydrogen-free and hydrogen-charged TWIP steels were examined with the aid of thorough electron microscopy, and hydrogen was demonstrated to promote twinning over slip–twin interactions. Based on the experimental findings, a microscale fracture model was proposed such that glide dislocations (or slip lines) and secondary twins distort the primary twin boundaries, and generate potential trap sites for hydrogen. The formation of nanotwins within the initially formed primary twins and the occurrence of slip dislocation pile ups finally lead to twin boundary cracking.

This new HE mechanism was incorporated into a VPSC model to account for HE. In addition, slip–twin and slip–grain boundary interactions in TWIP steels were also incorporated into VPSC, in order to capture the deformation response of the material in the presence of hydrogen. The simulation results both verify the success of the proposed HE mechanism for TWIP steels and constitute a potential design tool for applications requiring the utility of these superior materials in the presence of hydrogen.

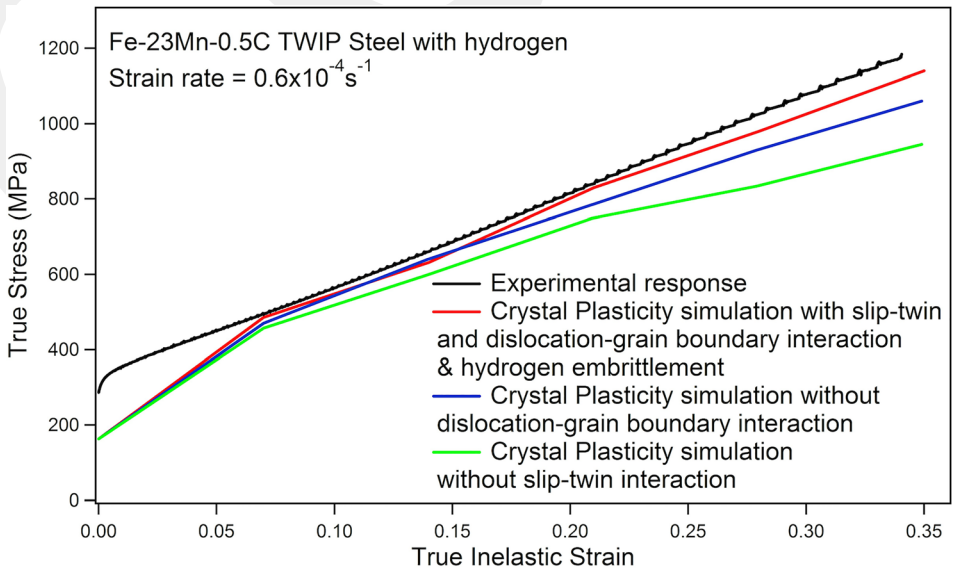

Fig. 13 Visco-plastic self-consistent simulations of the deformation response of Fe-23Mn-0.5C hydrogen-charged TWIP steel at 0.6×10^{-4} s^{-1}

Funding Data

- KAKENHI (Grant No. 15K18235).
- Japan Science and Technology Agency (JST) under Industry-Academia Collaborative R&D Program "Heterogeneous Structure Control: Towards Innovative Development of Metallic Structural Materials." (Grant No. 20100113).
- The Scientific and Technological Research Council of Turkey (TÜBİTAK) (Grant No. 112M806).

References

[1] Bouaziz, O., Allain, S., Scott, C. P., Cugy, P., and Barbier, D., 2011, "High Manganese Austenitic Twinning Induced Plasticity Steels: A Review of the Microstructure Properties Relationships," Curr. Opin. Solid State Mater. Sci., **15**(4), pp. 141–168.

[2] Bouaziz, O., Allain, S., and Scott, C., 2008, "Effect of Grain and Twin Boundaries on the Hardening Mechanisms of Twinning-Induced Plasticity Steels," Scr. Mater., **58**(6), pp. 484–487.

[3] Bal, B., Gumus, B., Gerstein, G., Canadinc, D., and Maier, H. J., 2015, "On the Micro-Deformation Mechanisms Active in High-Manganese Austenitic Steels Under Impact Loading," Mater. Sci. Eng. A, **632**, pp. 29–34.

[4] Gumus, B., Bal, B., Gerstein, G., Canadinc, D., and Maier, H. J., 2016, "Twinning Activity in High-Manganese Austenitic Steels Under High Velocity Loading," Mater. Sci. Technol., **32**(5), pp. 463–465.

[5] Rahman, K. M., Vorontsov, V. A., and Dye, D., 2015, "The Effect of Grain Size on the Twin Initiation Stress in a TWIP Steel," Acta Mater., **89**, pp. 247–257.

[6] Hamada, A. S., Karjalainen, L. P., and Puustinen, J., 2009, "Fatigue Behavior of High-Mn TWIP Steels," Mater. Sci. Eng. A, **517**(1–2), pp. 68–77.

[7] Lee, S., Kim, J., Lee, S.-J., and De Cooman, B. C., 2011, "Effect of Nitrogen on the Critical Strain for Dynamic Strain Aging in High-Manganese Twinning-Induced Plasticity Steel," Scr. Mater., **65**(6), pp. 528–531.

[8] Lee, T., Koyama, M., Tsuzaki, K., Lee, Y. H., and Lee, C. S., 2012, "Tensile Deformation Behavior of Fe-Mn-C TWIP Steel With Ultrafine Elongated Grain Structure," Mater. Lett., **75**, pp. 169–171.

[9] Koyama, M., Sawaguchi, T., Lee, T., Lee, C. S., and Tsuzaki, K., 2011, "Work Hardening Associated With ε-Martensitic Transformation, Deformation Twinning and Dynamic Strain Aging in Fe-17Mn-0.6C and Fe-17Mn-0.8C TWIP Steels," Mater. Sci. Eng. A, **528**(24), pp. 7310–7316.

[10] Gumus, B., Bal, B., Gerstein, G., Canadinc, D., Maier, H. J., Guner, F., and Elmadagli, M., 2015, "Twinning Activities in High-Mn Austenitic Steels Under High-Velocity Compressive Loading," Mater. Sci. Eng. A, **648**, pp. 104–112.

[11] Allain, S., Chateau, J.-P., Bouaziz, O., Migot, S., and Guelton, N., 2004, "Correlations Between the Calculated Stacking Fault Energy and the Plasticity Mechanisms in Fe–Mn–C Alloys," Mater. Sci. Eng. A, **387–389**, pp. 158–162.

[12] Gutierrez-Urrutia, I., and Raabe, D., 2011, "Dislocation and Twin Substructure Evolution During Strain Hardening of an Fe–22 wt.% Mn–0.6 wt.% C TWIP Steel Observed by Electron Channeling Contrast Imaging," Acta Mater., **59**(16), pp. 6449–6462.

[13] Dumay, A., Chateau, J.-P., Allain, S., Migot, S., and Bouaziz, O., 2008, "Influence of Addition Elements on the Stacking-Fault Energy and Mechanical Properties of an Austenitic Fe–Mn–C Steel," Mater. Sci. Eng. A, **483–484**, pp. 184–187.

[14] Koyama, M., Sawaguchi, T., and Tsuzaki, K., 2013, "TWIP Effect and Plastic Instability Condition in an Fe-Mn-C Austenitic Steel," ISIJ Int., **53**(2), pp. 323–329.

[15] Dastur, Y. N., and Leslie, W. C., 1981, "Mechanism of Work Hardening in Hadfield Manganese Steel," Metall. Trans. A, **12**(5), pp. 749–759.

[16] Hamada, A. S., and Karjalainen, L. P., 2011, "Hot Ductility Behaviour of High-Mn TWIP Steels," Mater. Sci. Eng. A, **528**(3), pp. 1819–1827.

[17] Lambers, H.-G., Rüsing, C. J., Niendorf, T., Geissler, D., Freudenberger, J., and Maier, H. J., 2012, "On the Low-Cycle Fatigue Response of Pre-Strained Austenitic Fe61Mn24Ni6.5Cr8.5 Alloy Showing TWIP Effect," Int. J. Fatigue, **40**, pp. 51–60.

[18] Frommeyer, G., Brüx, U., and Neumann, P., 2003, "Supra-Ductile and High-Strength Manganese-TRIP/TWIP Steels for High Energy Absorption Purposes," ISIJ Int., **43**(3), pp. 438–446.

[19] Zhang, L., Liu, X., and Shu, K., 2011, "Microstructure and Mechanical Properties of Hot-Rolled Fe-Mn-C-Si TWIP Steel," J. Iron Steel Res. Int., **18**(12), pp. 45–64.

[20] Mittal, S. C., Prasad, R. C., and Deshmukh, M. B., 1994, "Effect of Hydrogen on Fracture of Austenitic Fe-Mn-Al Steel," ISIJ Int., **34**(2), pp. 211–216.

[21] Koyama, M., Akiyama, E., and Tsuzaki, K., 2012, "Effect of Hydrogen Content on the Embrittlement in a Fe-Mn-C Twinning-Induced Plasticity Steel," Corros. Sci., **59**, pp. 277–281.

[22] Koyama, M., Akiyama, E., Tsuzaki, K., and Raabe, D., 2013, "Hydrogen-Assisted Failure in a Twinning-Induced Plasticity Steel Studied Under In Situ Hydrogen Charging by Electron Channeling Contrast Imaging," Acta Mater., **61**(12), pp. 4607–4618.

[23] Koyama, M., Springer, H., Merzlikin, S. V., Tsuzaki, K., Akiyama, E., and Raabe, D., 2014, "Hydrogen Embrittlement Associated With Strain Localization in a Precipitation-Hardened Fe–Mn–Al–C Light Weight Austenitic Steel," Int. J. Hydrogen Energy, **39**(9), pp. 4634–4646.

[24] Koyama, M., Akiyama, E., and Tsuzaki, K., 2012, "Hydrogen Embrittlement in a Fe-Mn-C Ternary Twinning-Induced Plasticity Steel," Corros. Sci., **54**, pp. 1–4.

[25] Park, I. J., Jeong, K. H., Jung, J. G., Lee, C. S., and Lee, Y. K., 2012, "The Mechanism of Enhanced Resistance to the Hydrogen Delayed Fracture in Al-Added Fe-18Mn-0.6C Twinning-Induced Plasticity Steels," Int. J. Hydrogen Energy, **37**(12), pp. 9925–9932.

[26] Dieudonné, T., Marchetti, L., Wery, M., Chêne, J., Allely, C., Cugy, P., and Scott, C. P., 2014, "Role of Copper and Aluminum Additions on the Hydrogen Embrittlement Susceptibility of Austenitic Fe–Mn–C TWIP Steels," Corros. Sci., **82**, pp. 218–226.

[27] Kwon, Y. J., Lee, T., Lee, J., Chun, Y. S., and Lee, C. S., 2015, "Role of Cu on Hydrogen Embrittlement Behavior in Fe-Mn-C-Cu TWIP Steel," Int. J. Hydrogen Energy, **40**(23), pp. 7409–7419.

[28] Zan, N., Ding, H., Guo, X., Tang, Z., and Bleck, W., 2015, "Effects of Grain Size on Hydrogen Embrittlement in a Fe-22Mn-0.6C TWIP Steel," Int. J. Hydrogen Energy, **40**(33), pp. 10687–10696.

[29] Bai, Y., Momotani, Y., Chen, M. C., Shibata, A., and Tsuji, N., 2016, "Effect of Grain Refinement on Hydrogen Embrittlement Behaviors of High-Mn TWIP Steel," Mater. Sci. Eng. A, **651**, pp. 935–944.

[30] Canadinc, D., Sehitoglu, H., and Maier, H. J., 2007, "The Role of Dense Dislocation Walls on the Deformation Response of Aluminum Alloyed Hadfield Steel Polycrystals," Mater. Sci. Eng. A, **454–455**, pp. 662–666.

[31] Canadinc, D., Biyikli, E., Niendorf, T., and Maier, H. J., 2011, "Experimental and Numerical Investigation of the Role of Grain Boundary Misorientation Angle on the Dislocation-Grain Boundary Interactions," Adv. Eng. Mater., **13**(4), pp. 281–287.

[32] Karaman, I., Sehitoglu, H., Beaudoin, A. J., Chumlyakov, Y. I., Maier, H. J., and Tome, C. N., 2000, "Modeling the Deformation Behavior of Hadfield Steel Single and Polycrystals Due to Twinning and Slip," Acta Mater., **48**(9), pp. 2031–2047.

[33] Dancette, S., Delannay, L., Renard, K., Melchior, M. A., and Jacques, P. J., 2012, "Crystal Plasticity Modeling of Texture Development and Hardening in TWIP Steels," Acta Mater., **60**(5), pp. 2135–2145.

[34] Zhou, P., Liang, Z. Y., Liu, R. D., and Huang, M. X., 2016, "Evolution of Dislocations and Twins in a Strong and Ductile Nanotwinned Steel," Acta Mater., **111**, pp. 96–107.

[35] Michler, T., and Naumann, J., 2008, "Hydrogen Environment Embrittlement of Austenitic Stainless Steels at Low Temperatures," Int. J. Hydrogen Energy, **33**(8), pp. 2111–2122.

[36] Bal, B., Koyama, M., Gerstein, G., Maier, H. J., and Tsuzaki, K., 2016, "Effect of Strain Rate on Hydrogen Embrittlement Susceptibility of Twinning-Induced Plasticity Steel Pre-Charged With High-Pressure Hydrogen Gas," Int. J. Hydrogen Energy, **41**(34), pp. 15362–15372.

[37] Lebensohn, R. A., and Tomé, C. N., 1993, "A Self-Consistent Anisotropic Approach for the Simulation of Plastic Deformation and Texture Development of Polycrystals: Application to Zirconium Alloys," Acta Metall. Mater., **41**(9), pp. 2611–2624.

[38] Canadinc, D., Karaman, I., Sehitoglu, H., Chumlyakov, Y. I., and Maier, H. J., 2003, "The Role of Nitrogen on the Deformation Response of Hadfield Steel Single Crystals," Metall. Mater. Trans. A, **34**(9), pp. 1821–1831.

[39] Canadinc, D., Sehitoglu, H., Maier, H. J., and Chumlyakov, Y. I., 2005, "Strain Hardening Behavior of Aluminum Alloyed Hadfield Steel Single Crystals," Acta Mater., **53**(6), pp. 1831–1842.

[40] Biyikli, E., Canadinc, D., Maier, H. J., Niendorf, T., and Top, S., 2010, "Three-Dimensional Modeling of the Grain Boundary Misorientation Angle Distribution Based on Two-Dimensional Experimental Texture Measurements," Mater. Sci. Eng. A, **527**(21–22), pp. 5604–5612.

[41] Kocks, U. F., Tomé, C. N., and Wenk, H. R., 1998, *Texture and Anisotropy*, Cambridge University Press, New York.

[42] Sofronis, P., and Birnbaum, H. K., 1995, "Mechanics of the Hydrogen-Dislocation-Impurity Interactions—Part I: Increasing Shear Modulus," J. Mech. Phys. Solids, **43**(1), pp. 49–90.

[43] McCormick, P. G., and Ling, C. P., 1995, "Numerical Modelling of the Portevin-Le Chatelier Effect," Acta Metall. Mater., **43**(5), pp. 1969–1977.

[44] Estrin, Y., and McCormick, P. G., 1991, "Modelling the Transient Flow Behaviour of Dynamic Strain Ageing Materials," Acta Metall. Mater., **39**(12), pp. 2977–2983.

[45] Soare, M. A., and Curtin, W. A., 2008, "Single-Mechanism Rate Theory for Dynamic Strain Aging in fcc Metals," Acta Mater., **56**(15), pp. 4091–4101.

[46] McCormick, P. G., 1988, "Theory of Flow Localisation Due to Dynamic Strain Ageing," Acta Metall., **36**(12), pp. 3061–3067.

[47] Ling, C. P., and McCormick, P. G., 1990, "Strain Rate Sensitivity and Transient Behaviour in an Al Mg Si Alloy," Acta Metall. Mater., **38**(12), pp. 2631–2635.

[48] Bal, B., Gumus, B., and Canadinc, D., 2016, "Incorporation of Dynamic Strain Aging Into a Viscoplastic Self-Consistent Model for Predicting the Negative Strain Rate Sensitivity of Hadfield Steel," J. Eng. Mater. Technol., **138**(3), p. 031012.

[49] Soare, M. A., and Curtin, W. A., 2008, "Solute Strengthening of Both Mobile and Forest Dislocations: The Origin of Dynamic Strain Aging in fcc Metals," Acta Mater., **56**(15), pp. 4046–4061.

[50] Anjabin, N., Karimi Taheri, A., and Kim, H. S., 2013, "Simulation and Experimental Analyses of Dynamic Strain Aging of a Supersaturated Age Hardenable Aluminum Alloy," Mater. Sci. Eng. A, **585**, pp. 165–173.
[51] Narayanan, S., McDowell, D. L., and Zhu, T., 2014, "Crystal Plasticity Model for BCC Iron Atomistically Informed by Kinetics of Correlated Kinkpair Nucleation on Screw Dislocation," J. Mech. Phys. Solids, **65**, pp. 54–68.
[52] Kang, K., Yin, J., and Cai, W., 2014, "Stress Dependence of Cross Slip Energy Barrier for Face-Centered Cubic Nickel," J. Mech. Phys. Solids, **62**, pp. 181–193.
[53] Springer, F., Nortmann, A., and Schwing, C., 1998, "A Study of Basic Processes Characterizing Dynamic Strain Ageing," Phys. Status Solidi A, **170**(1), pp. 63–81.
[54] Ono, K., 1968, "Temperature Dependence of Dispersed Barrier Hardening," J. Appl. Phys., **39**(3), pp. 1803–1806.
[55] Bayley, C. J., Brekelmans, W. A. M., and Geers, M. G. D., 2006, "A Comparison of Dislocation Induced Back Stress Formulations in Strain Gradient Crystal Plasticity," Int. J. Solids Struct., **43**(24), pp. 7268–7286.